Analytical Model for the SOI Lateral Power Device With Step Width Technique and High-*k* Dielectric

Jiafei Yao, *Member, IEEE*, Yufeng Guo, *Member, IEEE*, Kemeng Yang, Lin Du, Jun Zhang, and Tian Xia

***Abstract*— An analytical model is proposed in this paper for optimizing the breakdown voltage (BV) and drift region doping concentration of a silicon-on-insulator (SOI) lateral power device with step width technique and high-*k* dielectric (SWHK device). By solving the 3-D Poisson equation, the analytical potential and the electric field distribution are investigated. The optimal width of the silicon region of each zone is calculated to obtain the maximum BV and optimal drift region doping concentration. The analytical results are well matched with the simulation results, confirming the validity of the present model. The proposed analytical model reveals the influence of step number and permittivity of high-*k* dielectric on the performances of the SWHK device and provides guidance for the optimal design of the SWHK device.**

***Index Terms*— Analytical model, breakdown voltage (BV), high-*k*, silicon-on-insulator (SOI), step width (SW).**

I. Introduction

THE silicon-on-insulator (SOI) lateral power device is widely used in intelligent power applications due to its high breakdown voltage (BV), high speed, small resistance, and reduced leakage current [1]–[5]. In order to improve the BV, an effective approach is to introduce several additional electric field peaks in the drift region, the structures including step doped (SD) drift region [6], [7], step thickness (ST) drift region [8], [9], step buried (SB) oxide layer [10], [11], and variable-*k* dielectric [12], [13]. With the proposal of new structures of SOI lateral power devices, studies on the corresponding analytical model of the devices have made great progress in recent years. Analytical models for BV and surface electric field are proposed to analyze the physical mechanism and guide the design of the devices [6], [9], [11], [13]–[17].

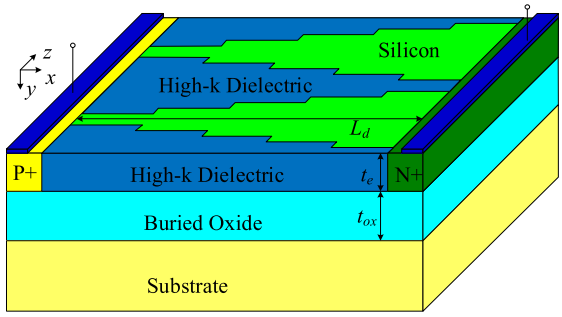

Fig. 1. 3-D view of the lateral power device with SWHK device.

To modulate the electric field in 3-D and improve the BV, the step width (SW) technique is proposed [18], [19]. The structure of the SOI lateral power device with SW technique and high-*k* dielectric (SWHK device) is shown in Fig. 1, the main feature of this structure is the interdigitated drift region using alternate silicon region and HK region. The width of the silicon region increases from source to drain stage, additional electric field peaks are generated at the steps, which results in a significant improvement of BV. Meanwhile, the high-*k* material is employed because of the enhancement of HK to the performance of the power devices [20], [22]. However, the SWHK device does not have detailed theoretical supports, and the electric field modulation effect in this device is not essentially explained. Hence, further investigation on this device is necessary to provide scientific basis and guidance for the design of such a device.

In this paper, a 3-D analytical model for the SOI lateral power device with SWHK is developed. This model provides a straightforward method to modulate the electric field distribution, improve the BV, and optimize the drift doping distribution. The 3-D device simulator Davinci is employed to simulate the numerical results, and the Mathematical software MATLAB is used to establish the analytical model. A good agreement between the analytical and numerical results is achieved, and the analytical results are well supported by the numerical simulations.

Manuscript received February 19, 2019; revised April 24, 2019 and April 29, 2019; accepted May 7, 2019. Date of publication May 30, 2019; date of current version June 19, 2019. This work was supported in part by the National Natural Science Foundation of China under Grant 61704084 and Grant 61574081, in part by the Natural Science Foundation of Colleges in Jiangsu Province under Grant 17KJB510042, in part by the Opening Foundation of State Key Laboratory of Electronic Thin Films and Integrated Devices under Grant KFJJ201704, and in part by the National and Local Joint Engineering Laboratory of RF Integration and Micro-Assembly Technology under Grant KFJJ20170302. The review of this paper was arranged by Editor F. Udrea. *(Corresponding author: Jiafei Yao.)*

J. Yao, Y. Guo, K. Yang, L. Du, and J. Zhang are with the National and Local Joint Engineering Laboratory of RF Integration and Micro-Assembly Technology, Nanjing University of Posts and Telecommunications, Nanjing 210023, China (e-mail: jfyao@njupt.edu.cn; yfguo@njupt.edu.cn).

T. Xia is with the School of Electrical Engineering, University of Vermont, Burlington, VT 05405 USA (e-mail: txia@uvm.edu).

Color versions of one or more of the figures in this paper are available online at http://ieeexplore.ieee.org.

Digital Object Identifier 10.1109/TED.2019.2916033

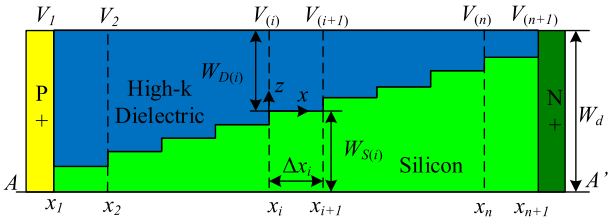

Fig. 2. Top view of one basic unit of the SWHK device.

TABLE I
SYMBOLS

Symbol	Description	Unit
t_e	thickness of epitaxial layer	μm
t_{ox}	thickness of buried oxide layer	μm
L_d	length of drift region	μm
N_d	doping concentration of drift region	cm^{-3}
W_d	width of drift region of basic unit	μm
W_S	width of silicon region	μm
W_D	width of dielectric region	μm
ε_{ox}	permittivity of oxide	F/cm
ε_s	permittivity of silicon	F/cm
ε_D	permittivity of dielectric	F/cm
q	Electric charge	C
V_B	reverse-bias voltage	V
Ec	critical electric field	V/cm

II. Analytical Model for the Electric Field and Verification

A. Electric Field Model

The cross section from the top view of one basic unit is shown in Fig. 2. The drift region between a P+ region and an N+ region with length L_d is equally divided into n zones with frame length $\Delta x_i = L_d/n$. Note that the step number should be $n-1$. $W_{S(i)}$ is the width of the n-type silicon region, and $W_{D(i)}$ is the width of the dielectric region in the i zone. Some symbols used in this paper are given in Table I.

A coordinate axis is established in each zone, x represents the horizontal position relative to the left edge of the zone, y represents the vertical position relative to the surface of the drift region, and z represents the width position relative to the interface of silicon and dielectric.

When a high reverse-bias voltage V_B is applied, the drift region is completely depleted. The potential function $\varphi_{S(i)}(x,y,z)$ in silicon and $\varphi_{D(i)}(x,y,z)$ in the dielectric region of i zone satisfy the 3-D Poisson equation, yielding

$$\frac{\partial^2\varphi_{S(i)}(x,y,z)}{\partial x^2}+\frac{\partial^2\varphi_{S(i)}(x,y,z)}{\partial y^2}+\frac{\partial^2\varphi_{S(i)}(x,y,z)}{\partial z^2}=-\frac{qN_d}{\varepsilon_S}$$
$$x_i \le x \le x_{i+1},\quad 0 \le y \le t_e,\quad -W_{S(i)} \le z \le 0 \tag{1}$$
$$\frac{\partial^2\varphi_{D(i)}(x,y,z)}{\partial x^2}+\frac{\partial^2\varphi_{D(i)}(x,y,z)}{\partial y^2}+\frac{\partial^2\varphi_{D(i)}(x,y,z)}{\partial z^2}=0$$
$$x_i \le x \le x_{i+1},\quad 0 \le y \le t_e,\quad 0 \le z \le W_{D(i)}. \tag{2}$$

Assuming that $\varphi_{S(i)}(x,y,z)$ and $\varphi_{D(i)}(x,y,z)$ can be approximated by the second-order Taylor series expansion [6], [22] yields

$$\varphi_{S(i)}(x,y,z)\approx\varphi_{S(i)}(x,z)+y\frac{\partial\varphi_{S(i)}(x,z)}{\partial y}+\frac{y^2}{2}\frac{\partial^2\varphi_{S(i)}(x,z)}{\partial y^2} \tag{3}$$

$$\varphi_{D(i)}(x,y,z)\approx\varphi_{D(i)}(x,z)+y\frac{\partial\varphi_{D(i)}(x,z)}{\partial y}+\frac{y^2}{2}\frac{\partial^2\varphi_{D(i)}(x,z)}{\partial y^2}. \tag{4}$$

According to the continuity of electric flux density across the interface of the epitaxial layer and the buried oxide layer, the potential functions $\varphi_{S(i)}(x,y,z)$ and $\varphi_{D(i)}(x,y,z)$ satisfy the boundary conditions as follows:

$$\begin{cases}\partial\varphi_{S(i)}(x,0,z)/\partial y=\partial\varphi_{D(i)}(x,0,z)/\partial y=0\\ \partial\varphi_{S(i)}(x,t_e,z)/\partial y=\varphi_{S(i)}(x,t_e,z)\varepsilon_{\rm ox}/\varepsilon_S t_{\rm ox}\\ \partial\varphi_{D(i)}(x,t_e,z)/\partial y=\varphi_{D(i)}(x,t_e,z)\varepsilon_{\rm ox}/\varepsilon_D t_{\rm ox}.\end{cases} \tag{5}$$

With the substitution of (3) and (4) into (1) and (2) under the boundary conditions (5), the 3-D potential function can be reduced to 2-D surface potential functions as follows:

$$\frac{\partial^2\varphi_{S(i)}(x,z)}{\partial x^2}+\frac{\partial^2\varphi_{S(i)}(x,z)}{\partial z^2}-\frac{\varphi_{S(i)}(x,z)}{t_S^2}=-\frac{qN_d}{\varepsilon_s} \tag{6}$$
$$\frac{\partial^2\varphi_{D(i)}(x,z)}{\partial x^2}+\frac{\partial^2\varphi_{D(i)}(x,z)}{\partial z^2}-\frac{\varphi_{D(i)}(x,z)}{t_D^2}=0 \tag{7}$$

where $t_S=(t_e^2/2+t_{\rm ox}t_e\varepsilon_s/\varepsilon_{\rm ox})^{1/2}$ and $t_D=(t_e^2/2+t_{\rm ox}t_e\varepsilon_D/\varepsilon_{\rm ox})^{1/2}$ are defined as the characteristic thicknesses in the silicon and dielectric regions, respectively.

Along the z-axis, the potential functions $\varphi_{S(i)}(x,z)$ and $\varphi_{D(i)}(x,z)$ satisfy the continuities of the potential, electric field, and doping along the interface of the silicon and dielectric regions. The boundary conditions are defined as follows:

$$\begin{cases}[\partial\varphi_{S(i)}(x,z)/\partial z]_{z=-W_{S(i)}}=0\\ [\partial\varphi_{D(i)}(x,z)/\partial z]_{z=W_{D(i)}}=0\\ [\varphi_{S(i)}(x,z)]_{z=0}=[\varphi_{D(i)}(x,z)]_{z=0}\\ \varepsilon_s[\partial\varphi_{S(i)}(x,z)/\partial z]_{z=0}=\varepsilon_D[\partial\varphi_{D(i)}(x,z)/\partial z]_{z=0}\\ [\partial^2\varphi_{S(i)}(x,z)/\partial x^2]_{z=0}=[\partial^2\varphi_{D(i)}(x,z)/\partial x^2]_{z=0}.\end{cases} \tag{8}$$

When the drift region is completely depleted, the reverse-bias voltage V_B is sustained by each region. The potentials at the edge of i zone are defined as $V_{(i)}$ and $V_{(i+1)}$, yielding

$$\begin{cases}\varphi_S(x_i,z)=\varphi_D(x_i,z)=V_{(i)}\\ \varphi_S(x_{i+1},z)=\varphi_D(x_{i+1},z)=V_{(i+1)}.\end{cases} \tag{9}$$

Solving the potential functions (6) and (7) under the boundary conditions (8) and (9), the surface potential and electric field of each zone at x-direction along AA′ line are obtained as

$$\varphi_{S(i)}(x)=(V_{(i+1)}-\phi_{(i)})\frac{\sinh(x-x_i/T_{(i)})}{\sinh(\Delta x_i/T_{(i)})}+(V_{(i)}-\phi_{(i)})\frac{\sinh[(x_{i+1}-x)/T_{(i)}]}{\sinh(\Delta x_i/T_{(i)})}+\phi_{(i)} \tag{10}$$
$$E_{S(i)}(x)=\frac{V_{(i+1)}-\phi_{(i)}}{T_{(i)}}\frac{\cosh[(x-x_i)/T_{(i)}]}{\sinh(\Delta x_i/T_{(i)})}-\frac{V_{(i)}-\phi_{(i)}}{T_{(i)}}\frac{\cosh[(x_{i+1}-x)/T_{(i)}]}{\sinh(\Delta x_i/T_{(i)})} \tag{11}$$

with

$$\begin{cases}\phi_{(i)}=qN_dT_{(i)}^2\alpha_{(i)}/\varepsilon_s\\ T_{(i)}^2=1/\left[\alpha_{(i)}/t_S^2+(1-\alpha_{(i)})/t_D^2\right]\\ \alpha_{(i)}=1/[1+(W_{D(i)}/W_{S(i)})(\varepsilon_D/\varepsilon_S)].\end{cases}$$

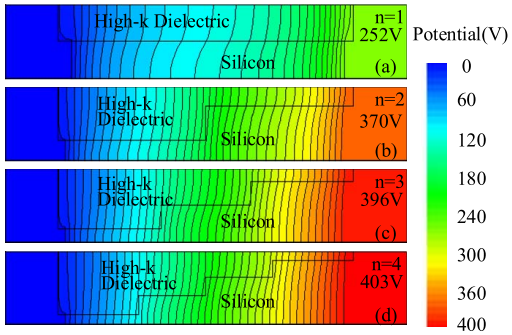

Fig. 3. Potential distribution for different device ($L_d = 20\ \mu$m, $W_d = 2\ \mu$m, $t_e = 1\ \mu$m, $t_{ox} = 3\ \mu$m, and $\varepsilon_D = 21$).

In each zone, T is defined as the equivalent characteristic thickness, α is a factor that depends on the width (W_D) and permittivity (ε_D) of the dielectric region. It is obvious that α decreases with the increasing of W_D or ε_D according to the formula. When $W_D = 0, \alpha$ equals to 1 and the equivalent characteristic thickness T equals to t_S, this case means no dielectric is used in the drift region, namely, the conventional lateral device [6].

$V_{(i)}$ can be solved by the continuities of the electric field $E_{S(i)}(x = x_i) = E_{S(i-1)}(x = x_i)$ and the boundary conditions, $V_{(1)} = 0$, expressed as

$$V_{(i)} = V_{(i+1)}A_{(i-1)} + B_{(i-1)}, \quad i = 1, \cdots, n \tag{12}$$

with

$$\begin{cases} A_{(i)} = E_{(i)}/(1 - E_{(i-1)}D_{(i)}/A_{(i-1)}), A_{(1)} = E_{(i)}, A_{(0)} = 0 \\ B_{(i)} = (B_{(i-1)}D_{(i)} + C_{(i)})/A_{(i)}, B_{(1)} = C_{(1)}, B_{(0)} = 0 \\ i = 2, \cdots, n-1 \end{cases}$$

and

$$\begin{cases} C_{(i)} = D_{(i)}\phi_{(i)}[\cosh(\Delta x_i/T_{(i)}) - 1] \\ \qquad + E_{(i)}\phi_{(i+1)}[\cosh(\Delta x_i/T_{(i+1)}) - 1] \\ D_{(i)} = 1/[(T_{(i)}/T_{(i+1)})\sinh(\Delta x_i/T_{(i)})\coth(\Delta x_i/T_{(i+1)}) \\ \qquad + \cosh(\Delta x_i/T_{(i)})] \\ E_{(i)} = 1/[\cosh(\Delta x_i/T_{(i+1)}) + (T_{(i+1)}/T_{(i)}) \\ \qquad \times \sinh(\Delta x_i/T_{(i+1)})\coth(\Delta x_i/T_{(i)})] \\ i = 1, \cdots, n-1. \end{cases}$$

Substituting the boundary conditions $V_{(n+1)} = V_B$, then $V_{(i)}$ is obtained. Actually, $V_{(i)}$ is equal to $V_B \cdot (i-1)/n$ when the reverse bias voltage V_B is sustained by each region averagely.

B. Verification and Discussions

To verify the proposed analytical model, numerical simulations were performed using the 3-D device simulator Davinci in 3-D coordinates. The comparisons between the SWHK devices with different steps ($n = 1$, $n = 2$, $n = 3$, and $n = 4$) are executed. The device with $n = 1$ means conventional HK device without steps. Fig. 3 shows the simulated equipotential contours for each device at their own optimal widths and maximum BV. For the HK device in Fig. 3(a), the potential lines are concentrated at the ends of the drift region but sparsely distributed in the middle of the drift region. The middle part of the drift region has not sustained the appropriate voltage, thus limiting the improvement of the BV. As shown in Fig. 3(b)–(d), the potential lines are uniformly distributed as the modulation of the steps, which means the reverse-bias voltage is averagely sustained by the drift region and a higher BV can be obtained.

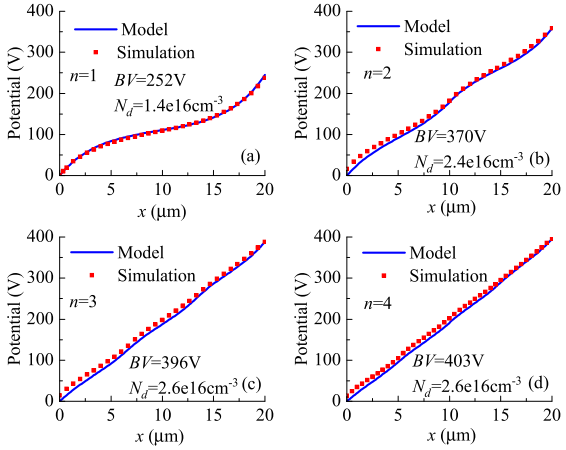

Fig. 4. Surface potential distributions along A-A′ Line for the SWHK devices with different n ($L_d = 20\ \mu$m, $W_d = 2\ \mu$m, $t_e = 1\ \mu$m, $t_{ox} = 3\ \mu$m, and $\varepsilon_D = 21$). (a) SWHK devices with $n = 1$, $W_{S(1)} = 1\ \mu$m. (b) SWHK devices with $n = 2$, $W_{S(1)} = 0.5\ \mu$m, $W_{S(2)} = 1.5\ \mu$m. (c) SWHK devices with $n = 3$, $W_{S(1)} = 0.35\ \mu$m, $W_{S(2)} = 1.0\ \mu$m, $W_{S(2)} = 1.65\ \mu$m. (d) SWHK devices with $n = 4$, $W_{S(1)} = 0.3\ \mu$m, $W_{S(2)} = 0.8\ \mu$m, $W_{S(2)} = 1.3\ \mu$m, $W_{S(4)} = 1.7\ \mu$m.

Fig. 4 gives the analytical and simulation results of the surface potential distributions along A-A′ Line for the SWHK devices with different n, the lines represent the analytical results of the proposed model established by MATLAB and the dots are the corresponding simulation results by the device simulator Davinci. A good agreement between the analytical model and simulation results can be found in general. As shown in Fig. 4(a), the maximum potential drop locates near the ends of the drift region, resulting in a high electric field peak at the junction. This limits the further improvement of the BV for the HK device. As shown in Fig. 4(b)–(d), the surface potential distribution approaches to linear dropping for the SWHK device, leading to a higher BV than the conventional HK device. Fig. 4 also indicates that the more step numbers bring better potential distribution.

Fig. 5 depicts the analytical and simulation results of the surface electric field distributions along A-A′ Line for the SWHK devices with different n. The agreement between the analytical and numerical results has circumstantiated the validity of the proposed model. As shown in the figure, new additional electric field peaks are introduced in the drift region for the SWHK devices, resulting in a higher BV compared with the conventional HK device without steps. The figure also indicates that with the increasing of the step number, a more uniform electric field is exhibited and a higher BV is achieved.

III. Optimal

According to the analytical and simulation results above, the steps bring new additional electric field peaks at the ends of each zone. To maximize the lateral BV, these new electric field peaks should be equal to the critical electric field (E_C) at the same time when a breakdown occurs [6]. Substituting (11) into $E_{S(i)}(x = x_i) = E_{S(i)}(x = x_{i+1}) = E_C$, the optimal width of each zone ($W_{S(i)\cdot\text{opt}}$) can be expressed as

$$W_{S(i)\cdot\text{opt}} = \frac{R(i)(\varepsilon_D/\varepsilon_S)}{[(\varepsilon_D/\varepsilon_S) - 1][R(i) - 1] + (\varepsilon_D/\varepsilon_S)/F(n)} W_d \tag{13}$$

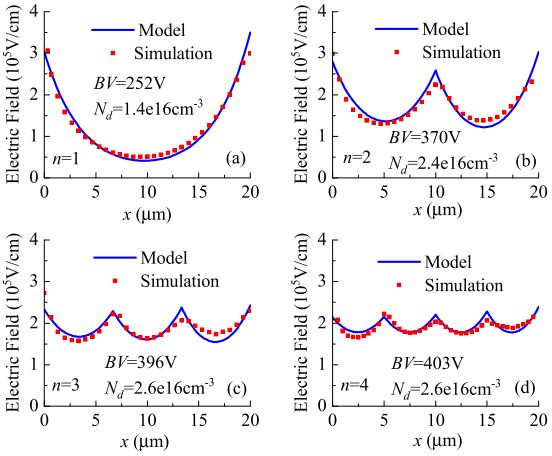

Fig. 5. Surface electric field distributions along A-A′ Line for the SWHK devices with different n ($L_d = 20\ \mu$m, $W_d = 2\ \mu$m, $t_e = 1\ \mu$m, $t_{ox} = 3\ \mu$m, and $\varepsilon_D = 21$). (a) SWHK devices with $n = 1$, $W_{S1} = 1\ \mu$m. (b) SWHK devices with $n = 2$, $W_{S1} = 0.5\ \mu$m, $W_{S2} = 1.5\ \mu$m. (c) SWHK devices with $n = 3$, $W_{S1} = 0.35\ \mu$m, $W_{S2} = 1.0\ \mu$m, $W_2 = 1.65\ \mu$m. (d) SWHK devices with $n = 4$, $W_{S1} = 0.3\ \mu$m, $W_{S2} = 0.8\ \mu$m, $W_{S2} = 1.3\ \mu$m, $W_{S4} = 1.7\ \mu$m.

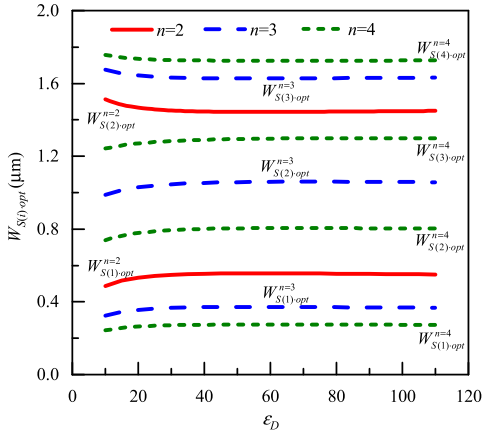

Fig. 6. Optimal $W_{S(i)\cdot opt}$ for the SWHK device with different n ($L_d = 20\ \mu$m, $W_d = 2\ \mu$m, $t_e = 1\ \mu$m, and $t_{ox} = 3\ \mu$m).

with

$$\begin{cases} R(i) = \dfrac{(2i-1)\tanh(0.5\Delta x_i/T_{(i)})/T_{(i)}}{\tanh(0.5\Delta x_i/T_{(1)})/T_{(1)}} \\ F(n) \\ \quad = \dfrac{\sqrt{4(\varepsilon_D/\varepsilon_S)^2 R(n)+(R(n)-1)^2}-[2(\varepsilon_D/\varepsilon_S)+R(n)-1]}{2[R(n)-1][(\varepsilon_D/\varepsilon_S)-1]} \end{cases}$$

the lateral BV (BV_{opt}) is expressed as

$$BV_{opt} = 2n \cdot E_C T_{(n)} \tanh(0.5L_d/nT_{(n)}) \tag{14}$$

and the optimal doping concentration ($N_{d\cdot opt}$) is expressed as

$$N_{d\cdot opt} = (2n-1)E_C\varepsilon_s \tanh(0.5L_d/nT_{(n)})/q\alpha_{(n)}T_{(n)}. \tag{15}$$

To obtain $W_{S(i)\cdot opt}$, the symbolic expressions of (13) is solved by the numeric approximation solution using MATLAB. Fig. 6 gives $W_{S(i)\cdot opt}$ for the SWHK devices with different n. As shown in the figure, $W_{S(i)\cdot opt}$ is almost constant when ε_D is larger than 20, which means the permittivity ε_D has minimal impact on $W_{S(i)\cdot opt}$.

Once $W_{S(i)\cdot opt}$ is obtained, the optimal BV BV_{opt} can be calculated by (14). Fig. 7 gives the analytical and simulation

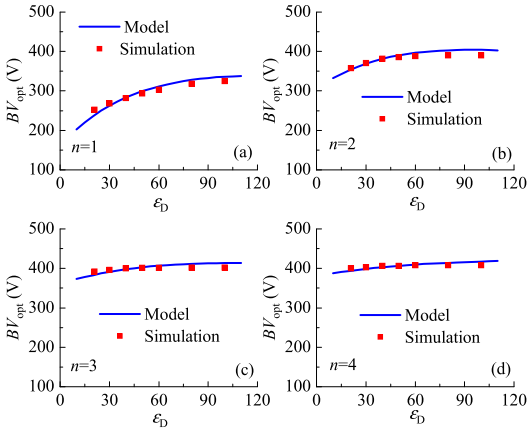

Fig. 7. Dependence of BV_{opt} on ε_D for the SWHK devices with different n ($L_d = 20\ \mu$m, $W_d = 2\ \mu$m, $t_e = 1\ \mu$m, and $t_{ox} = 3\ \mu$m).

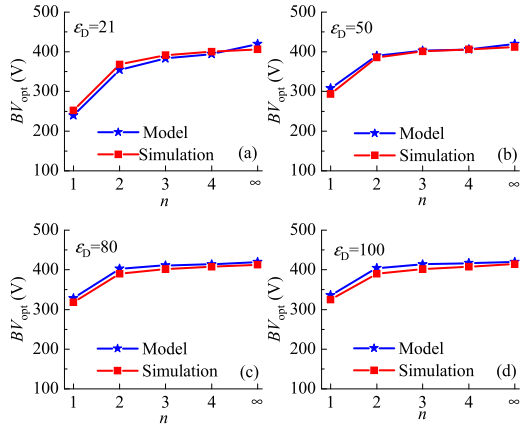

Fig. 8. Dependence of BV_{opt} on n for the SWHK devices with different ε_D ($L_d = 20\ \mu$m, $W_d = 2\ \mu$m, $t_e = 1\ \mu$m, and $t_{ox} = 3\ \mu$m).

results of BV_{opt} for the SWHK devices with different n. Similarly, the dots and curves show the numerical simulation results and analytical model, respectively. The analytical results are corresponding with the numerical simulations, proving the validity of the proposed model. As shown in this figure, BV_{opt} increases with the increase of ε_D, but the increment of BV_{opt} versus ε_D decreases with the increase of n. In Fig. 7(a), BV increases strongly because of the modulation of HK [23]. But for the SWHK device with $n = 4$, in Fig. 7(d), BV_{opt} increases gently with the increase of ε_D, this means that the BV of the SWHK device is not significantly affected by the dielectric permittivity. Therefore, a wide range of ε_D are available for the SWHK device. The potential high-k materials include HfO_2, $LaAlO_3$, Pr_2O_3, $ZrTiO_4$, TiO_2, and $SrTiO_3$ [24]–[29].

Fig. 8 shows the relation between the optimal BV BV_{opt} and the value n for the SWHK device. As shown in this figure, BV_{opt} of SWHK devices is higher than BV_{opt} of the conventional HK device ($n = 1$) with the same ε_D. Fig. 7 also indicates that BV_{opt} moderately increases with the increase of n, and it finally approaches a constant, because $\tanh(0.5L_d/nT)$ approximates to $0.5L_d/nT$ when n approaches infinity, then (14) can be written as $BV_{ideal} = E_C L_d$. This means that the BV will approach the ideal value of $E_C L_d$.

Fig. 9 gives the dependence of the calculated optimal drift doping concentration $N_{d\cdot opt}$ on the dielectric permittivity ε_D; along with the simulation results, the analytical results are also corresponding with the numerical simulations. Fig. 9 indicates that $N_{d\cdot opt}$ of SWHK devices are almost the same at the same

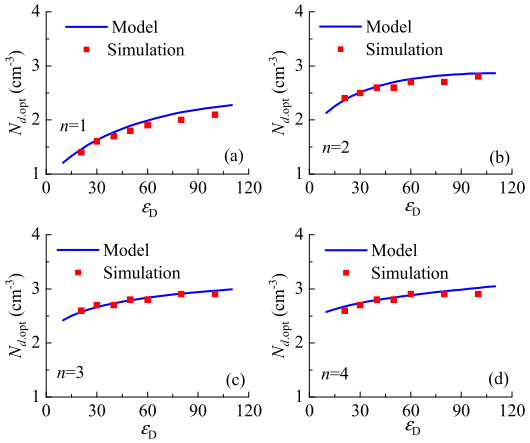

Fig. 9. Optimal N_d for the SWHK devices with different n ($L_d = 20$ μm, $W_d = 2$ μm, $t_e = 1$ μm, and $t_{ox} = 3$ μm).

ε_D, but they are higher than the $N_{d\cdot opt}$ of the conventional HK device at the same ε_D. As shown in the figure, $N_{d\cdot opt}$ increases with the increase in permittivity ε_D at a fixed number n, but the increment of $N_{d\cdot opt}$ versus ε_D also decreases with the increase of n, which means the more the steps, the less the effect of dielectric permittivity on the optimal drift doping concentration.

IV. Conclusion

An analytical model for the SOI lateral power device with SWHK is proposed in this paper. The analytical expressions of the potential and electric field distribution are obtained by solving the 3-D Poisson equation under specific boundary conditions. Then, the analytical results are verified by the numerical results obtained by the device simulator Davinci. Both the analytical and numerical results indicate that new additional electric field peaks are introduced in the drift region for the SWHK device, resulting in a higher BV than the conventional HK device without steps. Based on the analytical model, the widths of the silicon region of each zone are optimized to maximize the BV and doping concentration of the drift region. The analytical results of the optimal BV and doping concentration are in good agreement with the numerical results, confirming the validity of the present model in this paper. The results indicate that with the increase of the step numbers, the BV and doping concentration can be improved and the impact of the permittivity of HK on the performance of SWHK device can be reduced. This analytical model provides guidance for the optimal design of the SWHK device.

References

[1] F. Udrea, D. Garner, K. Sheng, A. Popescu, H. T. Lim, and V. I. Milne, "SOI power devices," *Electron. Commun. Eng. J.*, vol. 12, no. 1, pp. 27–40, Feb. 2000.

[2] S. Y. Liu, R. Ye, W. Sun, and L. X. Shi, "A novel lateral DMOS transistor with H-shape shallow-trench-isolation structure," *IEEE Trans. Electron Devices*, vol. 65, no. 11, pp. 5218–5221, Nov. 2018.

[3] W. Zhang *et al.*, "Non-full depletion mode and its experimental realization of the lateral superjunction," in *Proc. 30th ISPSD*, Chicago, IL, USA, May 2018, pp. 475–478.

[4] B. Yi, J. J. Cheng, and X. B. Chen, "A high-voltage 'Quasi-p-LDMOS' using electrons as carriers in drift region applied for SPIC," *IEEE Trans. Electron Devices*, vol. 33, no. 4, pp. 3363–3374, Apr. 2017.

[5] Y. N. Wang, Z. Wang, T. R. Bai, and J. B. Kuo, "Modeling of breakdown voltage for SOI trench LDMOS device based on conformal mapping," *IEEE Trans. Electron Devices*, vol. 65, no. 3, pp. 1056–1062, Mar. 2018.

[6] Y. F. Guo, Z. Li, and B. Zhang, "A new analytical model for optimizing SOI LDMOS with step doped drift region," *Microelectron. J.*, vol. 37, no. 9, pp. 861–866, Sep. 2006.

[7] Y. Hu, H. Wang, C. Du, M. Ma, M. Chan, J. He, and G. Wang, "A high-voltage (>600 V) N-Island LDMOS with step-doped drift region in partial SOI technology," *IEEE Trans. Electron Devices*, vol. 63, no. 5, pp. 1969–1976, May 2016.

[8] X. Luo, B. Zhang, Z. Li, W. Zhang, Z. Zhan, and H. Xu, "SOI high-voltage device with step thickness sustained voltage layer," *Electron. Lett.*, vol. 44, no. 1, pp. 55–56, Jan. 2008.

[9] X. Luo *et al.*, "Semiconductor science and technology a new SOI high-voltage device with a step-thickness drift region and its analytical model for the electric field and breakdown voltage," *Semicond. Sci. Technol.* vol. 23, no. 3, Feb. 2008, Art. no. 035028.

[10] B. Duan, B. Zhang, and Z. Li, "Breakdown voltage analysis for a double step buried oxide SOI structure," *Chin. J. Semicond.*, vol. 27, no. 5, pp. 886–891, May 2005.

[11] Y. Song, D. Baoxing, C. Zhen, G. Haijun, and Y. Yintang, "Analytical model of LDMOS with a double step buried oxide layer," *Solid-State Electron.*, vol. 123, pp. 6–14, Sep. 2016.

[12] X. R. Luo, F. Udrea, Y. G. Wang, G. L. Yao, and Y. Liu, "Partial SOI power LDMOS with a variable Low-κ dielectric buried layer and a buried P Layer," *IEEE Electron Device Lett.*, vol. 31, pp. 594–596, 2010.

[13] K. Zhou, X. Luo, Z. Li, and B. Zhang, "Analytical model and new structure of the variable-kDielectric trench LDMOS with improved breakdown voltage and specific on-resistance," *IEEE Trans. Electron Devices*, vol. 62, no. 10, pp. 3334–3340, Oct. 2015.

[14] X. Hu, B. Zhang, X. Luo, and Z. Li, "Analytical models for the electric field distributions and breakdown voltage of triple RESURF SOI LDMOS," *Solid-State Electron.*, vol. 69, pp. 89–93, Mar. 2012.

[15] Z. Cao, B. Duan, H. Cai, S. Yuan, and Y. Yang, "Theoretical analyses of complete 3-D reduced surface field LDMOS with folded-substrate breaking limit of Superjunction LDMOS," *IEEE Trans. Electron Devices*, vol. 69, no. 12, pp. 4865–4872, Dec. 2016.

[16] J. Zhang, Y.-F. Guo, and D. Z. Pan, "Effective concentration profile: Mechanism of gate field-plate assistant effect in SOI lateral power devices," *IEEE Electron Device Lett.*, vol. 65, no. 10, pp. 4476–4482, Oct. 2018.

[17] F. Udrea and D. Garner, "Lateral soi semiconductor device," U.S. Patent 0 120 187 A1, May 31, 2003.

[18] J.-F. Yao, Y.-F. Guo, J. Zhang, H. Lin, and X.-J. Xia, "Novel silicon-on-insulator lateral power device with step width drift region," *Superlattices Microstructures*, vol. 85, pp. 173–179, Sep. 2015.

[19] X. Chen and M. Huang, "A vertical power MOSFET with an interdigitated drift region using high-κ insulator," *IEEE Trans. Electron Devices*, vol. 59, no. 9, pp. 2430–2437, Sep. 2012.

[20] Y. Guo, J. Yao, B. Zhang, H. Lin, and C. Zhang, "Variation of lateral width technique in SoI high-voltage lateral double-diffused metal–oxide–semiconductor transistors using high-κ dielectric," *IEEE Electron Device Lett.*, vol. 36, no. 3, pp. 262–264, Mar. 2015.

[21] Y. Wang, X.-F. Mei, P.-P. Tang, and S.-F. Cui, "Analytical model and optimization for variable drift region width SOI LDMOS device," *IEEE Trans. Electron Devices*, vol. 63, no. 11, pp. 4352–4358, Nov. 2016.

[22] X. W. Wang *et al.*, "Mechanism and optimal design of a high-κ dielectric conduction enhancement SOI LDMOS," *Acta Phys. Sin.*, vol. 62, no. 23, 2013, Art. no. 237301.

[23] *Taurus Medici Davinci User Guide*, document Version D-2010.03, Mar. 2010.

[24] S. Subramaniam, S. M. Joshi, and R. N. Awale, "Suitability of high-κ gate dielectrics on the device performance and scalability of nanoscale double gate FINFETS with quantum modeling: A simulation study," *J. Electron Devices*, vol. 18, pp. 1582–1586, Oct. 2013.

[25] C.-W. Chang, C.-K. Deng, J.-J. Huang, H.-R. Chang, and T.-F. Lei, "High-performance poly-Si TFTs with Pr_2O_3 gate dielectric," *IEEE Electron Device Lett.*, vol. 29, no. 1, pp. 96–98, Jan. 2008.

[26] J. H. Park, G. S. Jang, H. Y. Kim, S. K. Lee, and S. K. Joo, "High-performance poly-Si thin-film transistor with high-κ $ZrTiO_4$ gate dielectric," *IEEE Electron Device Lett.*, vol. 36, no. 9, pp. 920–922, Sep. 2015.

[27] S. A. Campbell *et al.*, "MOSFET transistors fabricated with high permitivity TiO_2 dielectrics," *IEEE Trans Electron Devices*, vol. 44, no. 1, pp. 104–109, Jan. 1997.

[28] Z. Zhu, J. Xu, H. Zhao, and Z. Luo, "Conduction mechanism in $SrTiO_3$-based field-effect transistors," *IEEE Trans. Electron Devices*, vol. 62, no. 7, pp. 2352–2355, Jul. 2015.